Multi-scale assembly of hydrogels formed by highly branched arabinoxylans from *Plantago ovata* seed mucilage studied by USANS/SANS and rheology

Long Yu[1], Gleb E. Yakubov[1]*, Elliot P. Gilbert[2,3], Kim Sewell[4], Allison M.L. van de Meene[5] and Jason R. Stokes[1]

1. Australian Research Council Centre of Excellence in Plant Cell Walls, School of Chemical Engineering, The University of Queensland, Brisbane QLD 4076, Australia

2. Australian Centre for Neutron Scattering, Australian Nuclear Science and Technology Organisation, Sydney NSW 2232, Australia;

3. Australian Institute for Bioengineering and Nanotechnology and Queensland Alliance for Agriculture and Food Innovation, The University of Queensland, Brisbane QLD 4072, Australia

4. Centre for Microscopy and Microanalysis (CMM), The University of Queensland, Brisbane, QLD 4072, Australia

5. School of Biosciences, The University of Melbourne, Parkville VIC 3010, Australia

Highlights

34

35 • Multi-scale assembly of mucilage hydrogels from *Plantago ovata* seed is studied.

36 • A combination of small angle scattering and rheological techniques is used.

37 • Molecular structure and gel network are evaluated in non-gelled and gelled states.

38 • Hydrogen bonding contributes to gelation and distinct gel properties.

39

40

41

42

43

44

45

46

47

48

49

50

51

52

53

54

55

56

57

Abstract

The structures of two hydrogels formed by purified brush-like polysaccharides from *Plantago ovata* seed mucilage have been characterised from the nanometre to micrometre scale by using a combination of SANS and USANS techniques. These two hydrogels have distinctly different melting and rheological properties, but the structure of their gel networks bears striking similarity as revealed by USANS/SANS experiments. Surprisingly, we find that the dramatic changes in the rheological properties induced by temperature or change in the solvent quality are accompanied by a small alteration of the network structure as inferred from scattering curves recorded above melting or in a chaotropic solvent (0.7M KOD). These results suggest that, in contrast to most gel-forming polysaccharides for which gelation depends on a structural transition, the rheological properties of *Plantago ovata* mucilage gels are dependent on variations in intermolecular hydrogen bonding. By enzymatically cleaving off terminal arabinose residues from the side chains, we have demonstrated that composition of side-chains has a strong effect on intermolecular interactions, which, in turn, has a profound effect on rheological and structural properties of these unique polysaccharides.

1. Introduction

Mucilage hydrogel is a highly hydrated assembly of hydrophilic polysaccharides that forms a gel-like film around the seeds and roots of many plants (Western, 2012). Compared to other polysaccharide hydrocolloids, mucilage shows superior water holding capacity and swelling properties which in the wild is critical for the survival of plants in arid environments (Yang, Baskin, Baskin & Huang, 2012). These remarkable properties of natural mucilage are widely utilised in drug delivery applications, as well as in soil conditioning and food structure design (Di Marsico, Scrano, Amato, Gàmiz, Real & Cox, 2018; Fernandes & de las Mercedes Salas-Mellado, 2017; Haseeb, Hussain, Yuk, Bashir & Nauman, 2016). Further advances in these areas rest on the in-depth knowledge of the relationship between polysaccharide molecular conformation, assembly, microstructure, and the macroscopic properties of mucilage-based fluids and semi-solid materials.

Among many plant species producing mucilage, *Plantago ovata* seed mucilage exhibits a unique structure formed by a distinct layering of hydrogel materials around the seed (Yu et al., 2017). These hydrogels comprise a set of unusual arabinoxylans (AX) (or heteroxylans in some classifications) that are highly branched and contain atypical β-1$\rightarrow$3 linked Xyl in the side chains (Fischer, Yu, Gray, Ralph, Anderson & Marlett, 2004; Guo, Cui, Wang & Young, 2008). Previously, two AX fractions from different mucilage layers were isolated by step-wise extraction and we established that these AX fractions show markedly different gel properties but have similar molecular structure including molecular weight, monosaccharide and linkage compositions (Yu et al., 2017). Briefly, one of the polysaccharides (AX-W) is water soluble (hence 'W' in the label) and forms a weak thermosensitive gel, which melts at T $\sim$ 40 – 43 °C. The other isolated polysaccharide (AX-A) dissolves in alkaline solutions (hence 'A' in the label); in water, it forms a markedly stronger gel compared to AX-W. Concentrated ($\geq$1 wt%) AX-A gels retain their elastic behaviour (G'>G'') up to boiling temperature. If concentrations are lower (< 1 wt%) AX-A gels can be melted (G' $\approx$ G'') at around 85 °C. Both polysaccharides have Mw around 950 kDa with the average polydispersity index (M_w/M_n) of 1.5. The backbone of these AXs is β-1$\rightarrow$4 xylan; however, the degree of backbone substitution with side-chains exceeds 95 mol% of both AX fractions. Due to such high degree of backbone decoration with side chains, these polysaccharides can be classified as brush-like (or 'pipe-cleaner'-like) polymers. The overall Ara/Xyl ratio is 0.38 and 0.36 for AX-A and AX-W, respectively. A half of all xylose residues form the backbone, while another half, including β-1$\rightarrow$3 Xyl, is located within side chains. The estimated

4

121   Ara/Xyl ratio for the side chains is 0.75 and 0.70 for AX-A and AX-W, respectively. The

122   majority of side chains is estimated to be relatively short, i.e., from 1 to 3 sugar residues long.

123   We also note that detailed characterisation of protein admixtures, the content of bound ferulic

124   acid and its dehydrodimer form, as well as several other factors that may influence

125   rheological behaviour of AXs have been thoroughly evaluated and ruled out as possible

126   reason for the observed differences.

127   Due to similarity of linkage compositions and molecular weights of these two AX fractions,

128   the leading hypothesis proposed to explain differences in the gel properties was the variations

129   in side-chain distribution along the backbone, which may affect the strength of intra- and

130   inter-molecular hydrogen bonding. Recently, using small angle X-ray scattering and

131   rheological tests, the molecular associations of these arabinoxylans were explored in the non-

132   gelled state where hydrogen bonding is attenuated (see Supplementary Figure S1 for

133   reference) (Yu, Yakubov, Martínez-Sanz, Gilbert & Stokes, 2018). In that work, we have

134   established the link between hydrogen bonding and the degree of molecular association,

135   which enabled us to formulate the hypothesis that the nature of gel formation may also

136   depend on hydrogen bonding. That being said, the knowledge that hydrogen bonding drives

137   molecular association is insufficient to predict the structure of gel assemblies, since gel

138   formation may encompass or even require other structural transitions on the molecular (e.g.,

139   coil–helix (Schefer, Usov & Mezzenga, 2015)) and/or supra-molecular levels (e.g., bundle

140   formation (Jaspers, Pape, Voets, Rowan, Portale & Kouwer, 2016)).

141   To probe the gel structure of *P. ovata* mucilage AXs in a hydrated state, a combination of

142   ultra-small and small angle neutron scattering (USANS/SANS) was employed. This

143   combination of techniques has been used to investigate the hierarchical architecture of

144   bacterial cellulose hydrogels and enables the characterisation of polysaccharide hydrogels,

145   across multiple length scales covering at least four orders of magnitude: from < 10 Å

146   (molecular level) to > 10 µm (gel microstructure) (Martinez-Sanz et al., 2016). In addition,

147   this combination of scattering techniques was used to explore interaction mechanisms

148   between cellulose and other plant cell wall polysaccharides, which is particularly relevant for

149   the present work that seeks to evaluate interactions that drive gel formation in *P. ovata*

150   mucilage AXs (Martinez-Sanz et al., 2016).

151   The aim of this study is to investigate the assembly of *P. ovata* seed mucilage AX gels at

152   different length scales and to identify those structural elements that lead to differences in the

153 gel properties of compositionally similar AX fractions reported in our previous studies (Yu et
154 al., 2017). USANS/SANS is used to characterise the structural properties of mucilage
155 polysaccharides at varied temperatures and solvent conditions. The corresponding linear
156 viscoelastic properties are elucidated using small amplitude oscillatory shear rheometry.
157 Furthermore, the effect of side chains on molecular assembly is also investigated by
158 comparing the scattering patterns and rheological properties of intact polysaccharides and
159 their enzymatically modified counterparts.

2. Materials and methods

2.1 Materials

162 *P. ovata* seeds were provided by Dr Matthew Tucker (University of Adelaide, Australia). The
163 plant growth condition was based on a report of Phan et al. (2016). Briefly, the seeds are
164 sterilized with 50% ethanol and then washed with water before they are germinated on agar
165 plates at 22 °C/18 °C. After that, all seedlings were transplanted into the soil mixture and
166 grown in a glasshouse from December to March in Adelaide, Australia.

167 The D_2O and KOD solution were purchased from Sigma-Aldrich (Missouri, United States).
168 α-L-arabinofuranosidase was purchased from Megazyme (Bray, Ireland). All other chemicals
169 were of reagent grade. All water used in experiments was reverse osmosis treated water (DI
170 water) with resistivity of 18.2 MΩcm (Satorius Stedim).

2.2 Isolation of gel forming arabinoxylans from *P. ovata* seed mucilage

172 The mucilage fractions were prepared by stepwise extraction based on our previous work (Yu
173 et al., 2017). Briefly, *P. ovata* seeds were dispersed in 800 mL of DI water at 25 °C for 4 h
174 under constant stirring. The suspension was then centrifuged at 10,000 g for 30 min. The
175 remaining solid phase was dispersed in 400 mL of DI water at 65 °C for 4 h under constant
176 stirring. The suspension was then centrifuged at 10,000 g for 30 min. The resulting solution
177 was cooled to 4 °C to obtain a gel phase, which was then extensively dialysed against DI
178 water at 25 °C. The obtained hot water extracted fraction (AX-W) was freeze-dried and
179 stored for use in dry atmosphere until required. The remaining solid phase was dissolved in a
180 0.2 M KOH solution with 0.01 mg/mL $NaBH_4$ at 25 °C for 4 h, and the solution and residues
181 were separated by centrifugation. The resultant alkaline extract was dialysed at room
182 temperature for 48 h against DI water to obtain the so-called AX-A (alkaline extracted)
183 fraction, which was subsequently freeze-dried and stored for use in dry atmosphere until
184 required.

2.3 Preparation of mucilage solutions

The samples with 5% (w/w) concentration were prepared by dissolving the freeze-dried materials in D_2O at 65 °C for 6 h, and kept for the next 3h at 85 °C. Further, solutions were prepared by dissolving freeze-dried materials in alkali, which act as a mild hydrogen bonding inhibitor. As shown in Supplementary Figure S1 for data from our previous work (Yu et al., 2017), 1% AXs (w/v) behave like a gel, viscoelastic liquid and viscous liquid in H_2O, 0.2 M KOH and 8M guanidine hydrochloride solutions, respectively. To increase the scattering contrast between the solvent and polysaccharides, KOD - a deuterated version of KOH – was used as an alkaline solvent.

2.4 Rheological characterisation: steady shear and small amplitude oscillatory shear (SAOS) rheometry

The rheological tests were performed on an AR G2 rheometer (TA Instruments, USA) at 25 °C with a Peltier temperature control unit on bottom plate. After loading the sample, the edge of the geometry was carefully trimmed and filled with low viscosity silicone oil to prevent the possible water evaporation. The samples were left to rest for 5 min before each measurement. The parallel plate with 40 mm diameter and 0.5 mm of gap were used in all the tests. For the SAOS tests, the stress sweep measurements were completed at 1 Hz to determine stress values within the linear viscoelastic region. A frequency sweep in the range 10-0.01 Hz within the linear viscoelastic regime was subsequently performed for all samples. The typical strain value used for gel samples in D_2O is 1%, while the typical strain value used for samples in KOD is 20%.

2.4 Scanning Electron Microscopy

2.4.1 High Pressure Freezing Cryogenic Scanning Electron Microscopy (Cryo-SEM)

The method of Aston et al. (2016) is adapted for the sample preparation and cryogenic scanning electron microscopy (Cryo-SEM) imaging. The hydrogel samples (5 wt% AX-A and AX-W in H_2O) are prepared by high pressure freezing. For each hydrogel, a piece of sample is punch-cut from the gel using the base of a metal specimen carrier (Bal-Tec freeze-fracture brass platelets, 2 mm diameter). Hexadecane is used to occupy the voids within the carrier. The specimen carrier is then loaded into the high pressure freezer (Bal-Tec 010), where sample is rapidly frozen by a jet of high pressure (>2100 bar) liquid nitrogen. Thereafter the frozen samples are immediately transferred and stored in liquid nitrogen. Before Cryo-SEM imaging, the well-frozen dome of sample is exposed by carefully separating the lid and the base of the specimen carrier under liquid nitrogen using a custom

218   made "hat remover". The base with sample is placed on a holder (Gatan Alto, ALT 136) and

219   transferred under vacuum into the cold preparation-chamber (Gatan Alto, 2500) of SEM.

220   Inside preparation-chamber, the sample is fractured with a knife (Gatan precision cold rotary

221   fracture knife, ALT 335) to expose a clean surface, and then was coated with Pt at 10 mA for

222   120 s at around 5-10 nm thickness. The Cryo-SEM imaging is conducted using JEOL JSM-

223   7100F SEM at acceleration voltage of 2 kV.

224   ### 2.4.2 Slush freezing Cryogenic Scanning Electron Microscopy (Cryo-SEM)

225   Small, thin layer spreads of 5 wt% AX-A, AX-W and AX-W-E (enzymatically treated AX-W

226   fraction) gel samples in D_2O were placed on the specimen holder for the cold preparation-

227   chamber (Gatan Alto, 2500). The samples on the holder were rapidly frozen in a semi-solid

228   nitrogen slush before being placed in the Gatan Alto cryo-chamber using the transfer rod.

229   Once in the cryo chamber, the samples were fractured using a cold (-140 °C) to reveal the

230   internal substructure of the gel. The fractures were as close to the surface of the sample

231   holder as possible to minimise signs of ice crystal damage. After fracturing, the sample

232   holder temperature was raised to -95 °C and the samples etched for 2 minutes to sublime

233   excess water and reveal the structure of the sample. The samples were cooled again to -140

234   °C and sputter coated with gold-palladium. The samples were then transferred into an FEI

235   Qanta scanning electron microscope equipped with a cryo-stage. At least three different

236   fractures were imaged to obtain representative results.

237   ### 2.5 Small angle neutron scattering and ultra-small angle neutron scattering

238   Small angle neutron scattering (SANS) measurements were performed on the 40 m

239   QUOKKA instrument at the OPAL reactor (Gilbert, Schulz & Noakes, 2006; Wood et al.,

240   2018). Three configurations were used to cover a q range of 0.004–0.8 Å^{-1}, where q is the

241   magnitude of the scattering vector defined as $q=(4\pi/\lambda)\sin\theta$, and λ is the wavelength in Å and

242   2θ is the scattering angle. These configurations were: (i) source-to-sample distance (SSD) =

243   20 m, sample-to-detector distance (SDD)=20 m, (ii) SSD=12 m, SDD=12 m, (iii) SSD=12 m,

244   SDD=1.3 m using a wavelength, λ, of 5 Å of 10% resolution. The 5% AXs samples in D_2O or

245   0.7 M KOD were loaded in sealed 1mm path length cells with demountable quartz windows

246   (diameter 20 mm) and left overnight before testing. The data were reduced using NCNR SANS

247   reduction macros (Kline, 2006) modified for the QUOKKA instrument, using the Igor software

248   package (Wavemetrics, Lake Oswego, OR) with data corrected for empty cell scattering,

249   transmission, and detector sensitivity. The data were transformed onto an absolute scale using

250   attenuated direct beam transmission measurements.

251   Ultra-small angle neutron scattering (USANS) experiments were performed on the same samples
252   studied with SANS, using the KOOKABURRA instrument at the OPAL reactor (Rehm, Brûlé,
253   Freund & Kennedy, 2013; Rehm, Campo, Brûlé, Darmann, Bartsch & Berry, 2018). All samples
254   were loaded in the demountable KOOKABURRA sample cells with the path lengths of 1 mm and
255   the cross-section of 50 x 50 mm.

256   Using a neutron wavelength of 4.74 Å and a Cd aperture with a diameter of 35 mm, a q-range of
257   ca. 0.00003–0.007 Å^{-1} was accessed. Rocking curve profiles were measured by rotating the
258   analyser crystal away from the aligned peak position (the position at which the undeviated
259   neutrons are reflected onto the detector) and measuring the neutron intensity as a function of q.
260   The USANS data were reduced with an empty cell as background and converted onto an absolute
261   scale using adapted python scripts based on NCNR USANS reduction macros (Kline, 2006). The
262   reduced slit-smeared data were desmeared using the Lake algorithm before merging with the
263   SANS data (Kline, 2006).

3. Results and discussion

3.1 Multi-scale assembly of *P. ovata* arabinoxylan gel network

266   The *P.ovata* AX gels can be characterised by a porous microstructure typical of polymer and,
267   more specifically, polysaccharide gels. Figure 1 shows cryo-SEM images of AX-A and AX-
268   W 5 wt% gels prepared in H_2O (a complimentary set of lower resolution images of 5 wt%
269   gels prepared in D_2O is presented in Supplementary Figure S2). As seen from cryo-SEM data,
270   the microstructure of AX-A and AX-W gels is similar. The presence of larger clusters of
271   pores in AX-W sample (indicated by a circle in Figure 1D) may indicate more heterogeneous
272   network, which can be consistent with lower strength of AX-W gels. However, due to
273   softness of AX network artefacts associated with ice formation (even under conditions of
274   high pressure) may have significant impact on our ability to discern fine details of the gel
275   structure. To overcome sample preparation challenges of the imaging techniques, the
276   structure of fully hydrated mucilage hydrogels is probed using a combination of SANS and
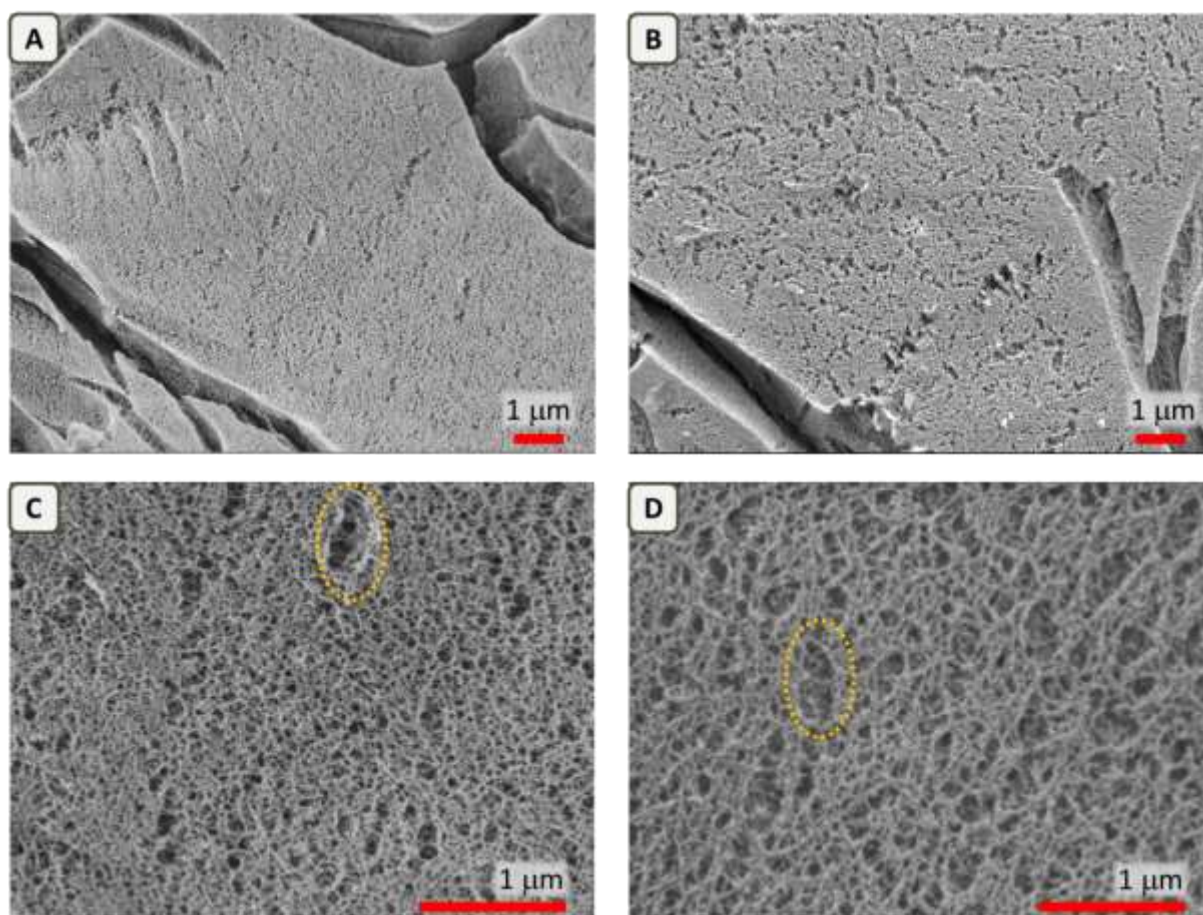277   USANS techniques.

Figure 1. SEM images of 5% AX-A ('A' and 'C') and AX-W ('B' and 'D') fraction in H_2O. A complimentary set of lower resolution images in D_2O is presented in Supplementary Figure S2. A, B are taken at 10'000 magnification; C, D are taken at 30'000 magnification. In all images, the scale bar is 1 μm. The dashed circle in 'C' and 'D' indicate presence of large pores, which either can indicate the level of gel heterogeneity or else potential artefacts of the high pressure freezing process.

282

283   The USANS/SANS combination enables probing the structure in the range of scattering

284   vectors, q, from 0.8 to $3 \cdot 10^{-5}$ Å^{-1}, which corresponds to length scales spanning at least four

285   orders of magnitude, *i.e.* from ~0.8 nm to ~20 μm. Overall, the scattering of AX-A and AX-

286   W fractions are found to be similar as shown in Figure 2A, which presents the overlapped

287   scattering curve obtained from SANS and USANS. The scattering patterns of both fractions

288   reveal three power law regions, $I(\mathbf{q}) \sim q^{-n}$, distinct from the background ($0.2 < q < 0.8$ Å^{-1}).

289   The region $0.02 < q < 0.2$ Å^{-1} corresponds to the length scales ~3 – 30 nm. In our previous

290   study, the radius of gyration of the AX-W fraction and AX-A fraction were determined to be

291   43 nm and 51 nm, respectively (Yu et al., 2017). Accordingly, at length scales ~3 – 30 nm,

292   the scattering curve reflects the molecular conformation of AX chains. The low q region

293   ($5 \cdot 10^{-4} < q < 0.01$ Å^{-1}), which spans the length scales from ~30 to 1260 nm, is characterised

294 by the power exponent of 3.5. The value of the exponent exceeds the number of physical
295 dimensions (D = 3), and can be observed in cases where scattering intensity is dominated by
296 the scattering from rough surfaces of 3D objects (a so-called 'surface fractal') (Sinha, Sirota,
297 Garoff & Stanley, 1988; Teixeira, 1988). For surface fractals, the scattered intensity, I(q),
298 scales with the scattering vector as $q^{-(6-D_f)}$, where D_f is the fractal dimension of the rough
299 (or irregular) 3D surface (Mildner & Hall, 1986). In polymer systems, the surface fractal-like
300 scattering can reflect the roughness of pores or irregularity of the pores with within the
301 biphasic gel network, or else can reflect the boundary between polymer-rich and polymer-
302 poor phases (Cherny, Anitas, Osipov & Kuklin, 2017; Hammouda, 2010; Ricciardi et al.,
303 2005). The ultra-low q region ($3 \cdot 10^{-5} < q < 3 \cdot 10^{-4}$ Å^{-1}), which corresponds to the
304 microstructure of the gels ($\sim 2 - 20$ μm), is dominated by the scattering typical of mass
305 fractals ($1 < n < 3$).

306 Based on the scattering patterns and complimentary SEM images, the deduced multi-scale
307 assembly of *Plantago* AXs from the molecular level up to gel network is shown in Figure 2B.
308 In order to illustrate our interpretation of "pore roughness" region, where I(q) $\sim q^{-3.3-3.6}$, we
309 have utilised SEM data to help visualising how pores can scatter at different length scales.
310 Figure 2B illustrates how a cluster of smaller pores transforms into a progressively larger
311 pore structure with the fractal dependency of the perimeter length on the size of a 'yardstick'.

312 Despite overall similarity, marked differences between the fractions can be identified by
313 examining the Kratky plot of the USANS/SANS data shown in Figure 2C. At ultra-low q
314 values ($3 \cdot 10^{-5} < q < 3 \cdot 10^{-4}$ Å^{-1}) the scattering from the AX-A fraction shows a more negative
315 (higher absolute value) power law exponent compared to the AX-W fraction, *i.e.* 2.6 and 1.9,
316 respectively. For mass fractals, the higher power law exponent indicates a more compact
317 structure, and thus we can infer that the microstructure of the AX-A fraction is more compact
318 than that of AX-W fraction. This interpretation finds further support from the SEM data;
319 which were used to perform the image-based fractal analysis using the cube-counting method
320 implemented in the Gwyddion microscopy data processing software (Nečas & Klapetek,
321 2012). The calculated fractal dimensions for the AX-A and AX-W fractions are found to be
322 2.5 and 2.3 respectively, which is consistent with trends observed in SANS. Another
323 difference between AX-A and AX-W fractions is observed in the medium q region ($q < 0.02$
324 Å^{-1}), where a small shift in the position of the minimum of I($\mathbf{q}$)$\cdot q^2$ (Figure 1C) has been
325 identified. This shift indicates that the scattering from fractal-like pores in the AX-A fraction

326 extend to slightly smaller size compared to the AX-W fraction, which is consistent with the

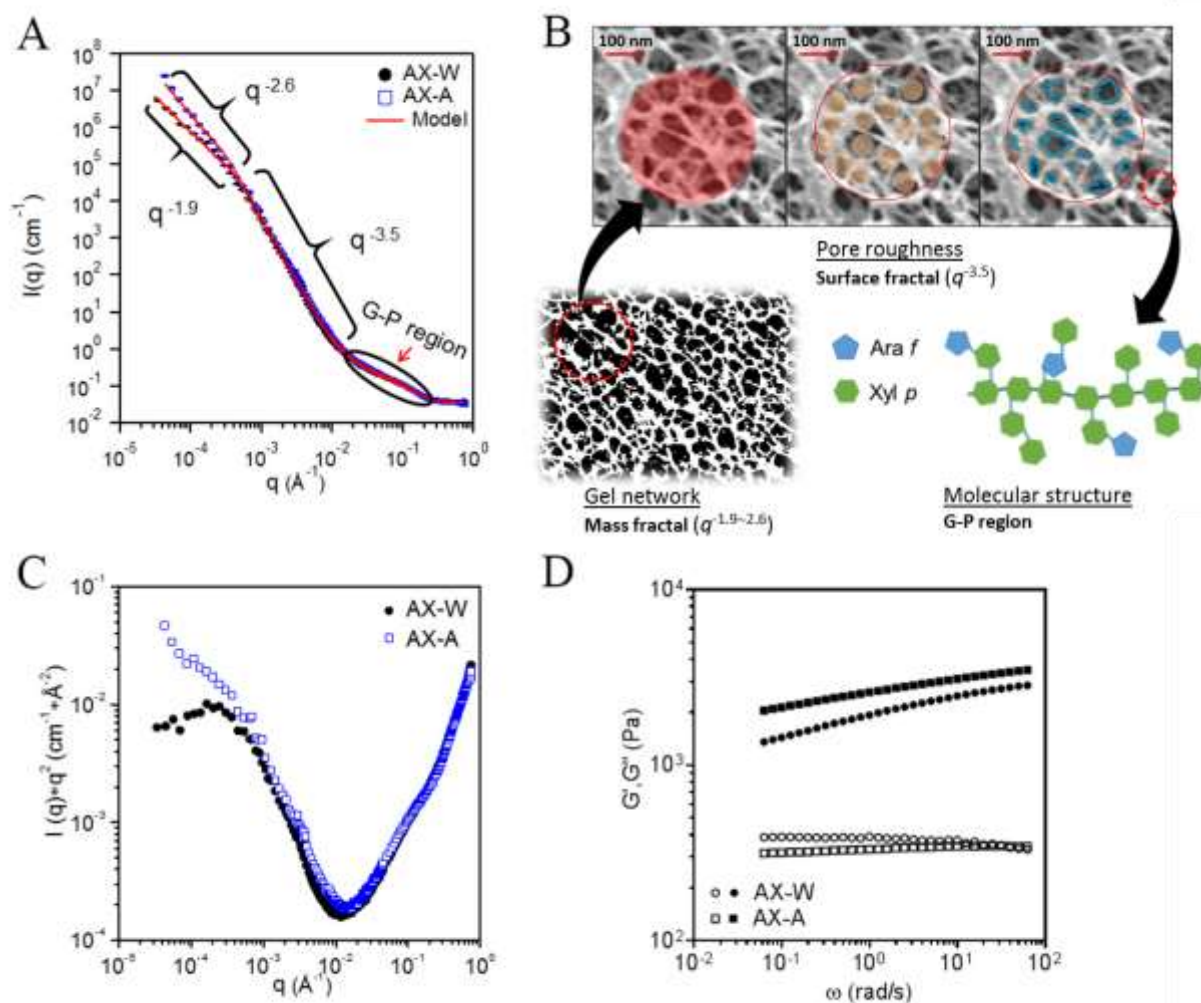327 pore sizes observed in the SEM images (Figure 1).

Figure 2. Characterisation of 5% AX-W fraction and AX-A fraction in D_2O. A: Combined SANS and USANS curves. Red lines represent fits to the two power law-Guinier-Porod (G-P) model. B: Proposed structural model of AX gels; the shaded area depicts a section of the three dimensional fractal that illustrates the proposed 'rough' pore model. C: Kratky plot of combined SANS and USANS data shown in panel A. D: SAOS frequency spectra; solid symbols represents G' and open symbols represents G".

328

329 To quantitatively describe the scattering data, we have utilised a model that combines two

330 power law functions with a Guinier-Porod model. The Guinier-Porod model is applied to

331 describe the high and medium q regions, while the two power laws describe the 'surface

332 fractal' and 'mass fractal' regions at low and ultra-low q, respectively. As shown in Figure

333 2A, the model provides a good fit, with fitting parameters summarised in Table 1. In the

334 Guinier-Porod model, the Porod exponent is fixed to 4, which represents the scattering from

335 'smooth surface' that is assigned to the interface between polymer chain and solvent. The

336 dimension variable reflects the 'shape' of scattering entities; in limiting cases of spherical and

337 rod-like scatterers the dimension variable assumes the values 0 and 1, respectively (Ricciardi

338 et al., 2005). As can be seen in Table 1, the local conformation of both fractions is rod-like as

339 expected for semi-flexible bottle-brush-like polymer chains at the nanometre scale. We note

340 that compared to AX-A fraction, the AX-W fraction has a lower radius of gyration (R_g), and

341 the larger value of the dimension variable, which is closer to unity. Since R_g represents a

342 dimension, independent of shape, the Guinier-Porod model inherently captures information

343 on the lateral and cross-sectional radius of polymer chains (~ 5 – 10 Å). We infer therefore

344 that the AX-A fraction has a larger cross-section compared to the AX-W fraction; this

345 difference may stem from the differences in the patterns of side-chain distribution or

346 architecture in these two AX fractions.

347

348 **Table 1.** Fitting parameters of combined two power law and Guinier-Porod model to the
349 USANS/SANS from AX-A fraction in D_2O at 25 °C, AX-W fraction in D_2O at 25, 70 and
350 80 °C, and AX-W-E (enzymatically treated AX-W fraction) in D_2O at 25 °C.

	AX-A 25 °C	AX-W 25 °C	AX-W 70 °C	AX-W 80 °C	AX-W-E 25 °C
Power law scale	0.000078(7) [a]	0.029(3)	0.0012 (2)	0.00043(7)	0.00547(2)
Ultra-low q exponent	2.62(1)	1.86(1)	2.24(2)	2.40(2)	1.734(5)
Low q exponent	3.472(3)	3.452(5)	3.301(8)	3.348(7)	3.570(3)
Crossover q (Å^{-1})	0.00073(2)	0.000431(6)	0.000330(9)	0.000276(8)	0.00156(1)
Guinier Scale	0.0158(3)	0.0088(1)	0.0055(2)	0.0052(2)	0.0127(3)
Dimension Variable	0.796(6)	0.943(5)	1.03(1)	1.04(1)	0.69(1)
Radius of gyration (Å)	8.66(7)	6.83(6)	6.2(2)	6.4(2)	7.8(1)
Porod Exponent	4(fixed)	4(fixed)	4(fixed)	4(fixed)	4(fixed)
Background (cm^{-1})	0.03564(6)	0.03657(6)	0.0397(2)	0.0377(1)	0.04589 (6)

351   a: Standard deviations on the last digit are shown in parentheses.

352 The crossover q value at which the scattering transitions from 'surface fractal' to 'mass

353 fractal' can be utilised to estimate the length scale of network heterogeneities, which would

354 include any large pores or pore clusters. As shown in Table 1, the AX-A fraction has twice as

355 high a crossover q compared to the AX-W fraction, indicating a smaller scale of

356 heterogeneities corresponding to ~0.86 μm in the AX-A gel as compared to ~1.46 μm in the

357 AX-W gel.

358 As shown in Figure 2D, the values of G' and G" of both fractions are very similar, although

359 the AX-A fraction has lower G" but higher G' values with a lower dependence on frequency,

360 and is thus a slightly more solid-like gel than the AX-W fraction. This result is consistent

361 with the interpretation of the USANS/SANS data, since a more solid gel is anticipated to

362 have a more compact structure and lower pore size at the same polymer concentration.

363 ## 3.2 Network structure under non-gelled and gelled states

364 In order to probe the relationship between the static structure probed by scattering and the

365 dynamic response probed in rheological tests, the gels were melted or dissolved using thermal

366 and alkali treatments, respectively.

367 Previously, we have shown that sensitivity to temperature is a hallmark feature of the AX-W

368 fraction in H_2O (Yu et al., 2017). The thermo-sensitivity of AX-W fraction is also found in

369 D_2O. As shown in Figure 3A, G' and G'' decrease while the value of tan δ (tan δ =G"/G')

370 increases with increasing temperature, which suggests a decrease in gel elasticity. The

371 thermal sensitivity of the AX-W hydrogel is more dramatic than the AX-A hydrogel; the

372 former melts with increasing temperature, with tan δ reaching unity at ∼ 80 °C (see insert in

373 Figure 3A).
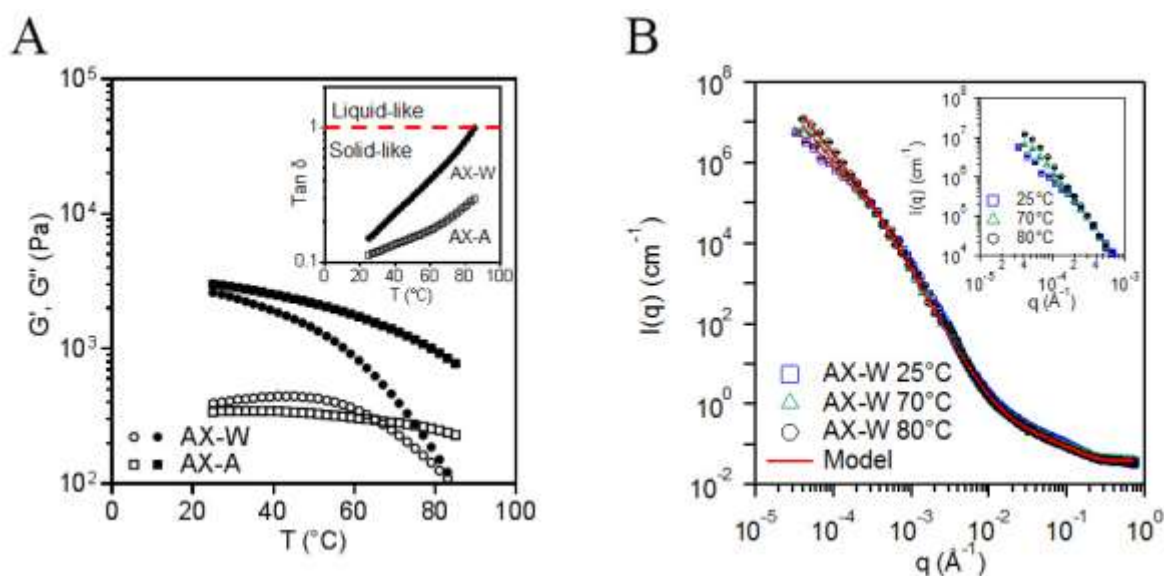
Figure 3. SAOS (A) of 5% (w/w) AX-W and AX-A from 25 °C to 85 °C (Filled symbols represent G' and empty symbols represents G". The insets is the plot of tan δ against T), and SANS (B) of 5% (w/w) AX-W fraction at 25, 70 and 80 °C (Red solid lines represent fits with the two power law plus Guinier-Porod model. The inset is ultra-low *q* region of the same data.).

374

To investigate the temperature induced structural changes, USANS and SANS were employed to probe the gels' structural features at 25, 70 and 80 °C. As shown in Figure 3B, the scattering curves from the AX-W fraction do not exhibit a significant change in the q range from 10^{-4} to 0.8 Å^{-1}. Some deviations are observed in the ultra-low q region ($< 10^{-4}$ Å^{-1}, see insert in Figure 3B). The fitting parameters to the two power law and Guinier-Porod model are summarized in Table 1. The Guinier-Porod parameters and low q power law exponent of the AX-W fraction at different temperatures are very similar, which suggests that the molecular conformation and the pore structure of the gel network do not change with temperature. The power law exponent at ultra-low q does, however, increases from 1.8 at 25°C to 2.4 at 80°C, which indicates the structure becomes more compact at high temperature. With increasing temperature, there is a decrease in the value of crossover q, suggesting that the region of the curve dominated by the scattering from the fractal-like pores extends to larger sizes. Therefore, whilst the gel strength decreases as AX-W gel becomes more fluid-like with increasing temperature, the overall structural arrangement remains the same. The variations at the micrometre length scale (> 6 µm) can be attributed to heterogeneity of larger-scale microstructure. For AX-A gels the temperature dependence is much weaker as shown in Figure 3A. Accordingly, their scattering patterns measured at different temperatures practically overlap as shown in Supplementary Figure S3.

Besides temperature, mild alkaline environment (pH > 13) has a significant impact on rheological properties of AX fractions. Based on our previous results, an alkali, such as KOH or its deuterated version KOD, can solubilise *Plantago* AXs and abate gel formation (Yu, Yakubov, Martínez-Sanz, Gilbert & Stokes, 2018; Yu et al., 2017). In particular, it was established that 5 wt% solutions of both fractions in 0.2M KOH exhibit behaviour of entangled polymer solutions (Yu, Yakubov, Martínez-Sanz, Gilbert & Stokes, 2018). As shown in Figure 4A and C, both fractions behave as viscoelastic fluids in 0.7 M KOD, because the value of G" is higher that of G' with strong dependency on oscillatory frequency, ω, compared to that in D$_2$O. That being said, the two fractions in KOD do differ in the magnitude of the dynamic shear modulus G* (G*=$\sqrt{(G')^2 + (G'')^2}$) and the ratio of the viscous component of the modulus relative to the elastic one (*i.e.,* tan δ =G"/G') (See supplementary Figure S4). In addition, the two fractions show marked difference in the dependency of the dynamic shear moduli on ω. In particular, the 5 wt% AX-W fraction in KOD shows behaviour of a weakly viscoelastic fluid, whereby values of G" are at least an order of magnitude higher than G', and both moduli exhibit strong dependency on ω (Figure

408   4A). By contrast, the 5 wt% AX-A fraction in KOD exhibits a more pronounced viscoelastic

409   response (Figure 4C), which is further evidenced by the much lower value of tan δ compared

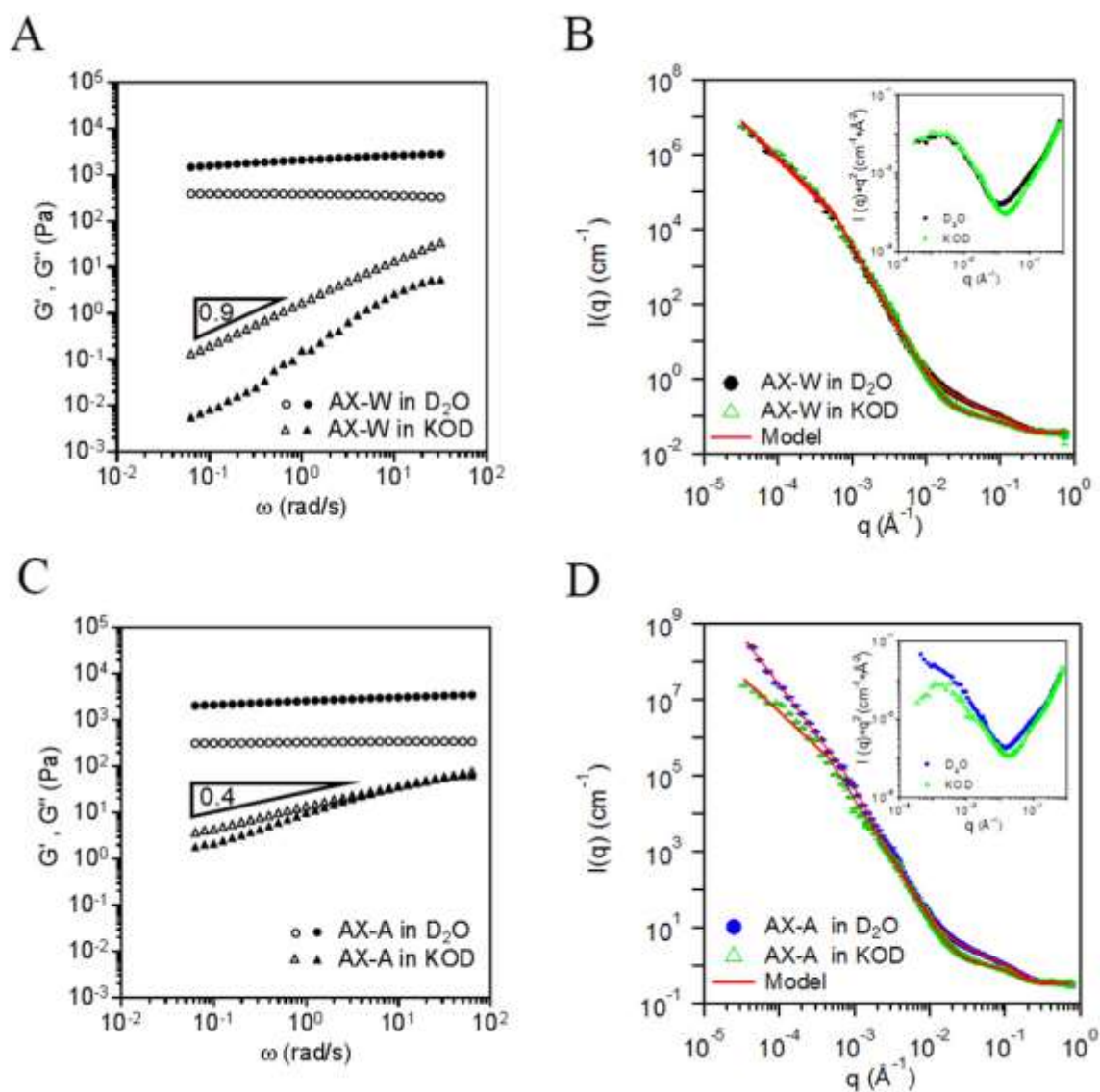410   to the AX-W fraction (Supplementary Figure S4A).

411

Figure 4. SAOS (A, C) (Filled symbols represent G' and empty symbols represents G", the plots of tan δ against ω and G* against ω are shown in supplementary Figure S3) and USANS/SANS (B, D) of AX-W and AX-A fractions in D_2O and 0.7 M KOD (Red solid lines represent fits to the two power law-Guinier Porod model). The insets in panels B and D are the corresponding Kratky plots, which assist in visualising differences between scattering profiles recorded under different solvent conditions.

412

16

413   To examine the key structural features associated with the solvent, the corresponding

414   scattering curves from the AX-W and AX-A fractions in both solvents are compared in

415   Figure 4C and 4D, respectively. The scattering curves for the AX-W fraction in D_2O and

416   KOD overlap very well in the low q region with small differences at medium q (0.01 to 0.1

417   Å^{-1}). In contrast, for the AX-A fraction, differences are observed in both the ultra-low q ($<$

418   10^{-4} Å^{-1}) and medium q regions (0.01 to 0.1 Å^{-1}).

419   The scattering data are fitted to a combined model (two power law and Guinier-Porod model)

420   with results summarised in Table 2. The differences in the scattering patterns of both

421   fractions in D_2O and KOD at medium q (0.01 to 0.1 Å^{-1}) are captured in the model by the

422   changes in the value of the Guinier-Porod dimension variable (s) and radius of gyration (R_g).

423   In D_2O, the dimension variable is close to 1 (rod-like scatterer), while in KOD, it is closer to

424   0 (sphere-like scatterer). We note that the dimension variable of the AX-A fraction is

425   particularly low ($s = 0.12$) compared to the AX-W fraction ($s = 0.45$). This result indicates

426   that on the length scales of 10 – 30 nm the chain of the AX-A fraction in KOD adopts a more

427   coiled or globular conformation, while AX-W, which is rod-like in D_2O (s = 0.94), retains a

428   more 'elongated' shape even when dissolved in KOD. In addition, the radius of gyration of

429   both fractions are markedly larger in KOD compared to D_2O, so that the cross-sectional area

430   of the scatterers ($\sim R_g^2$) increases 2.1 and 1.7 times for the AX-A and AX-W fractions,

431   respectively.

432

433   **Table 2.** Fitting parameters of combined two power law and Guinier-Porod model to the
434   USANS/SANS from AX-W and AX-A fraction in D_2O and KOD at 25 °C.

Parameters	5% AX-W fraction		5% AX-A fraction	
	0.7M KOD	D_2O	0.7M KOD	D_2O
Power law scale	0.012(1) [a]	0.029(3)	0.011(1)	0.000078(7)
Ultra-low q exponent	1.97(1)	1.86(1)	1.91(1)	2.62(1)
Low q exponent	3.517(5)	3.452(5)	3.188(4)	3.472(3)
Crossover q (Å^{-1})	0.000582(8)	0.000431(6)	0.000492(9)	0.00073(2)
Guinier Scale	0.0168(5)	0.0088(1)	0.054(2)	0.0158(3)
Dimension Variable	0.45(1)	0.943(5)	0.12(1)	0.796(6)
Radius of gyration (Å)	8.9(1)	6.83(6)	12.6(1)	8.66(7)
Porod Exponent	4(fixed)	4(fixed)	4(fixed)	4(fixed)
Background (cm^{-1})	0.03464(6)	0.03657(6)	0.03465(5)	0.03564(6)

435   a: Standard deviations on the last digit are shown in parentheses.

On the length scales exceeding the molecular dimensions, the scattering from both AX fractions in D_2O and KOD are similar, suggesting that the gel network in D_2O is structurally similar to that of the entangled polymer network in KOD. In the AX-A fraction, a slight decrease in the ultra-low and low q power law exponents, as well as a small decrease in the crossover q in KOD was observed (Table 2) which may indicate that the AX-A entangled polymer network is somewhat less compact in KOD compared to a gel network in D_2O.

The above results demonstrate that *P.ovata* mucilage hydrogels retain the key feature of their structure regardless of the gel strength or the transition from gelled to non-gelled states; this conclusion is particularly clear for the scattering curves recorded at different temperatures, where no changes in the medium q region were recorded. Previously, we demonstrated that hydrogen bonding is the key factor responsible for gelation; the SAXS and rheological results reported in Yu et al. (2018) suggest that the sol-gel transition of *Plantago* mucilage polysaccharides chiefly depends on the strength and/or distribution of hydrogen bonds within the system rather than the changes in the molecular structure (Yu, Yakubov, Martínez-Sanz, Gilbert & Stokes, 2018). Accordingly, the differences in strength and/or number of hydrogen bonds can be readily probed under conditions of oscillatory shear, whereby weak bonds yield and result in the rearrangement of the gel network necessary for enabling some degree of gel flow (probed by G"). By contrast, under static conditions of USANS/SANS/SAXS measurements, such disruptions and rearrangements may not be directly observable.

3.3 Hydrogen bonding mediated by side chains

The gel strength of the AX-W fraction (and not of the AX-A fraction) can be modulated by enzymatic cleavage of terminal arabinoses of the side chains using arabinofuranosidase. It has been hypothesised that, in the AX-W fraction, hydrogen bonding is linked to terminal arabinoses of the side chains, and hence their cleavage results in a drastic decrease in the gel strength of the AX-W fraction in H_2O (Yu et al., 2017). In this work we utilise the enzymatic cleavage to examine changes in the gel/polymer structure. Arabinofuranosidase enzyme was used to partially cleave terminal arabinose residues from the side chains of AX-W fraction to obtain a so-called AX-W-E fraction (Yu et al., 2017). The monosaccharide analysis reveals that the terminal arabinose residues of AX-W fraction are released after enzymatic treatment (see Supplementary Figure S5). As shown in Figure 5A, the dynamic moduli (G' and G") of the AX-W-E fraction are lower than for the AX-W fraction. While G' > G'' in both samples, the moduli have a significant dependence on frequency for the AX-W-E fraction that indicates the gel is much more fluid-like. Figure 5B shows the scattering curves of the AX-

469 W-E fraction and AX-W fraction, with fitting parameters summarized in Table 1. The Kratky

470 plot shown in Figure 5C is used to better visualise the differences between the samples.

471 The overall scattering pattern of the AX-W-E fraction is qualitatively similar to its original

472 counterpart. The Guinier-Porod parameters, such as dimension variable and R_g of the AX-W-

473 E fraction, only show small changes; this indicates that the loss of terminal arabinoses of the

474 side chains may not necessarily result in a dramatic effect on the chain conformation. Overall,

475 the decrease in the dimension variable may be linked to some degree of increased flexibility

476 induced by reduced length of side chains, which makes molecules appear less rod-like even

477 on the nanometre scale. Both power law exponents are similar for AX-W and AX-W-E

478 fractions; this suggests that the fractal-like features of the hydrogel network are largely

479 analogous.

480 The key changes correspond to the shift in the q-position of the crossover points; *i.e.* the

481 transition from the Guinier-Porod to the low-q power law, and the transition between the low-

482 q and ultra-low q power law exponents. The value of crossover q of the AX-W-E fraction is

483 three times higher than AX-W fraction, indicating a smaller-dimension transition from

484 surface fractal to mass fractal probably due to higher level of heterogeneities.

485 As shown in Figure 5D, in the panel that illustrates molecular level of structure, the terminal

486 arabinose residues in AX-W-E fraction are removed after enzymatic hydrolysis

487 (Supplementary Figure S5), and the molecule becomes somewhat more flexible because

488 steric effects from side chains are reduced. (Please note that treatment with

489 arabinofuranosidase does not change the degree of backbone decoration, because the cleaved

490 residues are terminal arabinoses attached to β-1→3 linked xylose residue, which are part of

491 an oligosaccharide side-chain). Such changes are further evidenced by variations in Guinier-

492 Porod parameters in response to enzymatic treatment. Furthermore, on a larger length scale,

493 the relatively more flexible polymer chains in AX-W-E fraction form smaller gel pores with

494 decreased roughness, compared to the AX-W fraction. Arguably, as shown in Table 1, the

495 AX-W-E fraction is characterised by a relatively higher value of the low q exponent ($n =$

496 $6 - D_{\text{surface fractal}}$) and the higher value of crossover q. Further, this hypothesis is evidenced
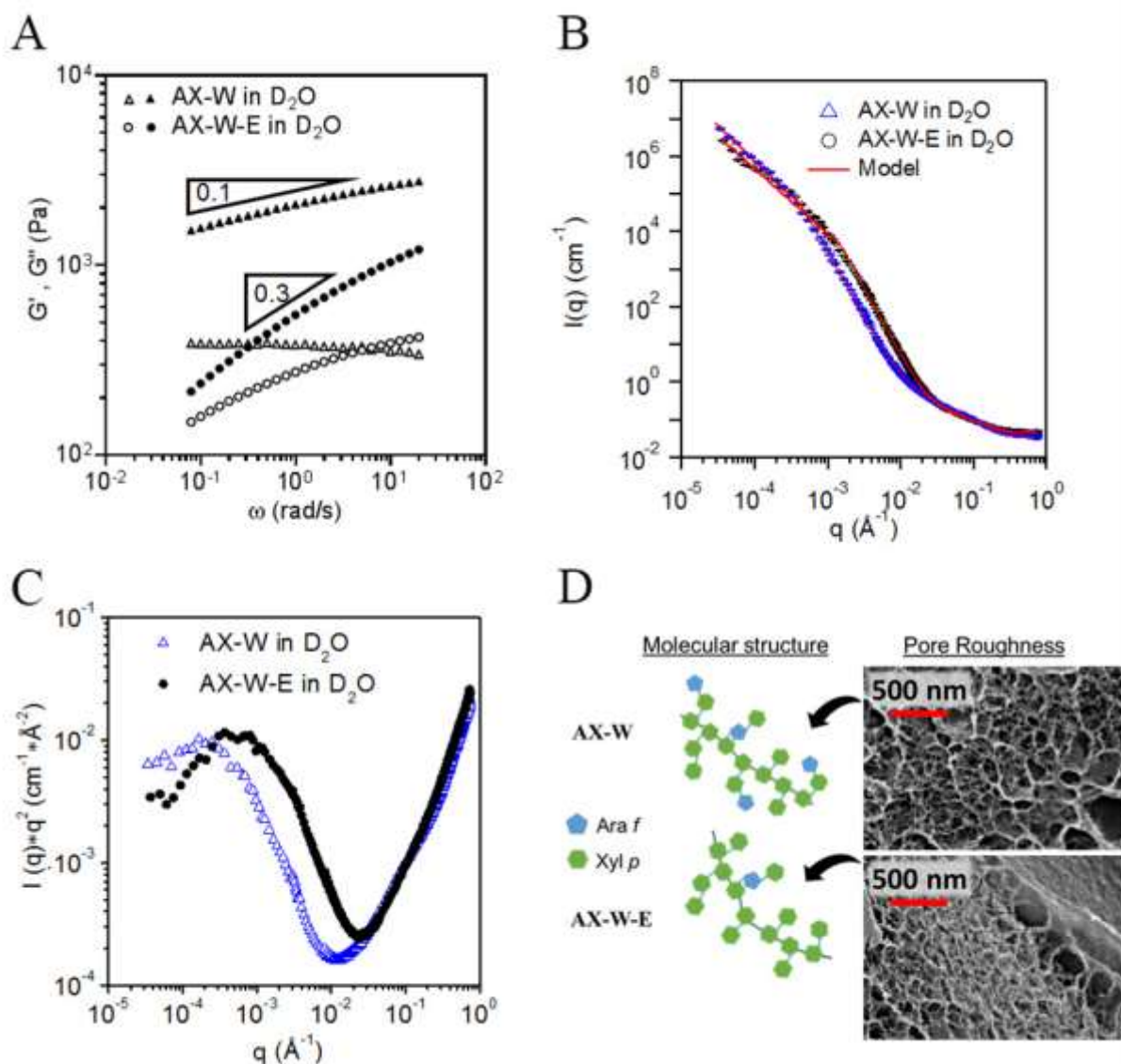
497 be the SEM data shown in figure 5D.

Figure 5. Characterisation of 5% AX-W fraction and its enzymatically treated counterpart (AX-W-E) in D_2O. A: SAOS frequency spectra; solid symbols represents G' and open symbols represents G". B: Combined SANS and USANS curves. Red lines represent fits to the two power law-Guinier-Porod model. C: The Kratky plot of combined SANS and USANS data shown in panel B. D: Comparison of pore structure of AX-W and AX-W-E gels based on SEM images in D_2O. The smaller pore radius of AX-W-E gels deduced from the Kratky plot is consistent with microscopy data.

498

499   These findings highlight the fact that xylose backbone of *P.ovata* AXs is heavily substituted;

500   the majority of terminal arabinoses (A_t) cleaved by arabinofuranosidase are a part of X-A_t or

501   X-X-A_t side chains. Upon cleavage, the side chines become shorter but remains attached to

502   the backbone. Previously, it has been shown that removal of decorations from β-1$\rightarrow$4 linked

503   xylan backbone results in formation of crystalline domains and poor solubility of cereal AXs

504   (Heikkinen, Mikkonen, Pirkkalainen, Serimaa, Joly & Tenkanen, 2013; Höije, Sternemalm,

Heikkinen, Tenkanen & Gatenholm, 2008; Shelat, Vilaplana, Nicholson, Wong, Gidley & Gilbert, 2010). Most direct evidence has been uncovered by Heikkinen et al. (2013), who demonstrated that wheat AX with similar Ara/Xyl ratio but different degree of arabinose distribution, show different degree of crystallinity. Those molecules that have lower level of decoration show prominent crystallisation, while molecules with similar A/X ratio but more evenly distributed pattern of arabinose side-chain decorations display markedly lower crystallinity. We, therefore, conclude that *P.ovata* AXs display a markedly different behaviour compared to cereal AXs, which is due to high level of backbone decoration and a more complex structure of side chains.

4. Conclusions

Using a combination of USANS and SANS we have probed the multi-scale assembly of AX gels from *P. ovata* seed mucilage. We show that the scattering patterns are dominated by pores and pore clusters, which have a broad distribution of sizes spanning from a few tens of nanometres up to a sub-micrometre scale. To determine the underpinning mechanism of gelation, we probed the static structure while modulating the rheological properties of gels by utilising the following conditions: increase of temperature, change of solvent quality using mild alkali, and enzymatic treatment. The results show that the static structure as probed by USANS/SANS may not fully reflect the rheological properties of gels.

Upon melting of gels at elevated temperatures, the scattering patterns show marginal change indicating that melting transition is not associated with structural re-arrangement of polymer network. However, temperature influences micro-scale heterogeneity of AX gels, as inferred from changes in the $I(q) \sim q^{-n}$ scaling at ultra-low q values ($3 \cdot 10^{-5} < q < 3 \cdot 10^{-4}$ Å^{-1}) accessed through the use of USANS. The transition from a gel state in D$_2$O to an entangled polymer viscoelastic liquid in chaotropic 0.7M KOD solvent elicited changes in chain conformation, which become more flexible. On the larger scale, the structure of gels and entangled solutions are largely analogous. Upon enzymatic hydrolysis, which alters the chemical structure of the chain, marked changes in rheological properties are observed that are accompanied by changes in the static structure of the polymer network, which features a smaller pore size and a less compact microstructure at the micrometre length scales. In striking contrast to cereal AXs, the removal of terminal arabinoses from AX-W fraction does not expose β-1→4 xylan backbone, which is due to a more complex structure of side chains as well as very small amounts of arabinose residues directly linked to the backbone. These features of *Plantago*

AXs may play an important physiological role in mucilage extrusion and its water holding capacity. Arguably, the use of side-chain decorations as a "mix-and-match" toolbox for creating different gel and coating materials based on a relatively simple set of chemical structures and their permutations can be an advantageous strategy for enhancing adaptability and mitigating environmental stresses.

To conclude, the gelation mechanism of mucilage polysaccharides from *P.ovata* seed mucilage is distinctly different from most polysaccharides (e.g., agarose) and is chiefly mediated by inter-chain hydrogen bonding. We hypothesise that this mechanism emerged due to the extremely high level of backbone decoration by side-chains (up to 95%), which inhibits interactions that involve sugar residues in the backbone. In addition, the way changes in the structure of side chain affect the structure and rheology should prompt future research focused on the detailed structural characterization of mucilage polysaccharides including side-chain length, their distribution and monomer sequences in order to unlock the structural origin of hydrogen bonding in this class of complex polysaccharides.

570

571

572

573

574

575

576

577

578

579

580

581

582

583

584

585

586

587

588

589

590

References

Aston, R., Sewell, K., Klein, T., Lawrie, G., & Grondahl, L. (2016). Evaluation of the impact of freezing preparation techniques on the characterisation of alginate hydrogels by cryo-SEM. *European Polymer Journal, 82*, 1-15.

Cherny, A. Y., Anitas, E., Osipov, V., & Kuklin, A. (2017). Scattering from surface fractals in terms of composing mass fractals. *Journal of applied crystallography, 50*(3), 919-931.

Di Marsico, A., Scrano, L., Amato, M., Gàmiz, B., Real, M., & Cox, L. (2018). Mucilage from seeds of chia (Salvia hispanica L.) used as soil conditioner; effects on the sorption-desorption of four herbicides in three different soils. *Science of The Total Environment, 625*, 531-538.

Fernandes, S. S., & de las Mercedes Salas-Mellado, M. (2017). Addition of chia seed mucilage for reduction of fat content in bread and cakes. *Food Chemistry, 227*, 237-244.

Fischer, M. H., Yu, N. X., Gray, G. R., Ralph, J., Anderson, L., & Marlett, J. A. (2004). The gel-forming polysaccharide of psyllium husk (Plantago ovata Forsk). *Carbohydrate Research, 339*(11), 2009-2017.

Gilbert, E. P., Schulz, J. C., & Noakes, T. J. (2006). 'Quokka'—the small-angle neutron scattering instrument at OPAL. *Physica B: Condensed Matter, 385*, 1180-1182.

Guo, Q., Cui, S. W., Wang, Q., & Young, J. C. (2008). Fractionation and physicochemical characterization of psyllium gum. *Carbohydrate polymers, 73*(1), 35-43.

Hammouda, B. (2010). A new Guinier–Porod model. *Journal of applied crystallography, 43*(4), 716-719.

Haseeb, M. T., Hussain, M. A., Yuk, S. H., Bashir, S., & Nauman, M. (2016). Polysaccharides based superabsorbent hydrogel from Linseed: Dynamic swelling, stimuli responsive on–off switching and drug release. *Carbohydrate polymers, 136*, 750-756.

Heikkinen, S. L., Mikkonen, K. S., Pirkkalainen, K., Serimaa, R., Joly, C., & Tenkanen, M. (2013). Specific enzymatic tailoring of wheat arabinoxylan reveals the role of substitution on xylan film properties. *Carbohydrate polymers, 92*(1), 733-740.

Höije, A., Sternemalm, E., Heikkinen, S., Tenkanen, M., & Gatenholm, P. (2008). Material Properties of Films from Enzymatically Tailored Arabinoxylans. *Biomacromolecules, 9*(7), 2042-2047.

Jaspers, M., Pape, A. C. H., Voets, I. K., Rowan, A. E., Portale, G., & Kouwer, P. H. J. (2016). Bundle Formation in Biomimetic Hydrogels. *Biomacromolecules, 17*(8), 2642-2649.

Kline, S. R. (2006). Reduction and analysis of SANS and USANS data using IGOR Pro. *Journal of applied crystallography, 39*(6), 895-900.

Martinez-Sanz, M., Mikkelsen, D., Flanagan, B. M., Rehm, C., de Campo, L., Gidley, M. J., & Gilbert, E. P. (2016). Investigation of the micro-and nano-scale architecture of cellulose hydrogels with plant cell wall polysaccharides: A combined USANS/SANS study. *Polymer, 105*, 449-460.

Mildner, D. F. R., & Hall, P. L. (1986). Small-angle scattering from porous solids with fractal geometry. *Journal of Physics D: Applied Physics, 19*(8), 1535.

Nečas, D., & Klapetek, P. (2012). Gwyddion: an open-source software for SPM data analysis. *Central European Journal of Physics, 10*(1), 181-188.

Phan, J. L., Tucker, M. R., Khor, S. F., Shirley, N., Lahnstein, J., Beahan, C., Bacic, A., & Burton, R. A. (2016). Differences in glycosyltransferase family 61 accompany variation in seed coat mucilage composition in Plantago spp. *Journal of Experimental Botany, 67*(22), 6481-6495.

Rehm, C., Brûlé, A., Freund, A. K., & Kennedy, S. J. (2013). Kookaburra: the ultra-small-angle neutron scattering instrument at OPAL. *Journal of applied crystallography, 46*(6), 1699-1704.

Rehm, C., Campo, L. d., Brûlé, A., Darmann, F., Bartsch, F., & Berry, A. (2018). Design and performance of the variable-wavelength Bonse–Hart ultra-small-angle neutron scattering diffractometer KOOKABURRA at ANSTO. *Applied Crystallography, 51*(1), 1-8.

Ricciardi, R., Mangiapia, G., Lo Celso, F., Paduano, L., Triolo, R., Auriemma, F., & Lauprêtre, F. (2005). Structural organization of poly (vinyl alcohol) hydrogels obtained by freezing and thawing techniques: A SANS study. *Chemistry of materials, 17*(5), 1183-1189.

Schefer, L., Usov, I., & Mezzenga, R. (2015). Anomalous Stiffening and Ion-Induced Coil-Helix Transition of Carrageenans under Monovalent Salt Conditions. *Biomacromolecules, 16*(3), 985-991.

643   Shelat, K. J., Vilaplana, F., Nicholson, T. M., Wong, K. H., Gidley, M. J., & Gilbert, R. G. (2010).
644   Diffusion and viscosity in arabinoxylan solutions: Implications for nutrition. *Carbohydrate polymers,*
645   *82*(1), 46-53.
646   Sinha, S., Sirota, E., Garoff, S., & Stanley, H. (1988). X-ray and neutron scattering from rough
647   surfaces. *Physical Review B, 38*(4), 2297.
648   Teixeira, J. (1988). Small-angle scattering by fractal systems. *Journal of applied crystallography,*
649   *21*(6), 781-785.
650   Western, T. L. (2012). The sticky tale of seed coat mucilages: production, genetics, and role in seed
651   germination and dispersal. *Seed Science Research, 22*(1), 1-25.
652   Wood, K., Mata, J., Garvey, C., Wu, C.-M., Hamilton, W., Abbeywick, P., & Booth, N. (2018).
653   QUOKKA, the pinhole small-angle neutron scattering instrument at the OPAL Research Reactor,
654   Australia: design, performance, operation and scientific highlights. *Applied Crystallography, 51*(2),
655   294-314.
656   Yang, X. J., Baskin, J. M., Baskin, C. C., & Huang, Z. Y. (2012). More than just a coating: Ecological
657   importance, taxonomic occurrence and phylogenetic relationships of seed coat mucilage. *Perspectives*
658   *in Plant Ecology Evolution and Systematics, 14*(6), 434-442.
659   Yu, L., Yakubov, G. E., Martínez-Sanz, M., Gilbert, E. P., & Stokes, J. R. (2018). Rheological and
660   structural properties of complex arabinoxylans from Plantago ovata seed mucilage under non-gelled
661   conditions. *Carbohydrate polymers, 193*, 179-188.
662   Yu, L., Yakubov, G. E., Zeng, W., Xing, X., Stenson, J., Bulone, V., & Stokes, J. R. (2017). Multi-
663   layer mucilage of Plantago ovata seeds: Rheological differences arise from variations in arabinoxylan
664   side chains. *Carbohydrate polymers, 165*, 132-141.

665

666

667
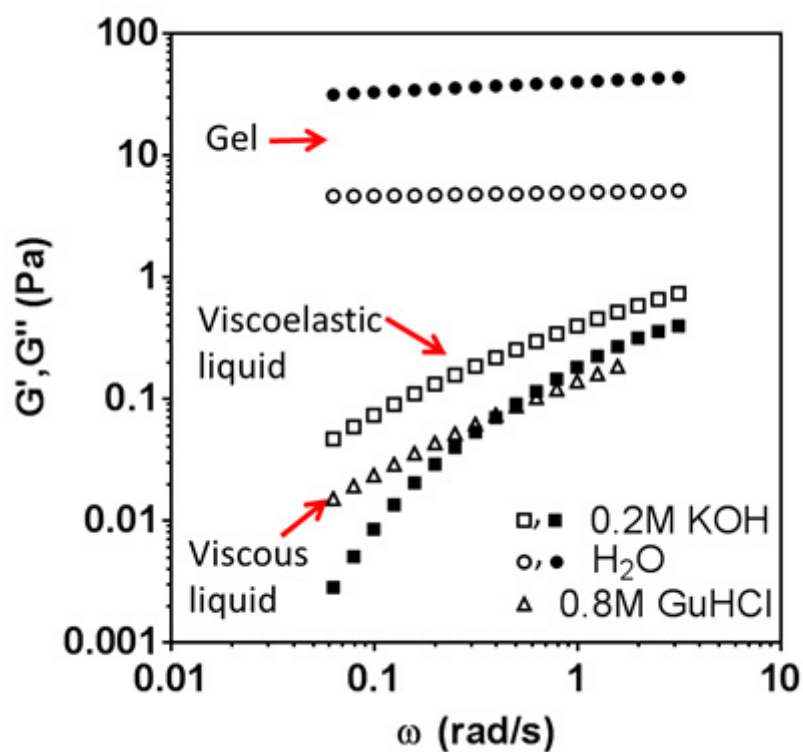
668

669

670

671

672

673

674

675

676

677

678

679

680

681
682

Supplementary material

Supplementary Figure S1. Rheological properties of AX-A from *P. ovata* seed mucilage in 0.2 M KOH, 8M GuHCl and H_2O. G' for AX-A in GuHCl was negligible. Solid symbols represents G' and open symbols represents G". Adapted from Yu et al. (2017).
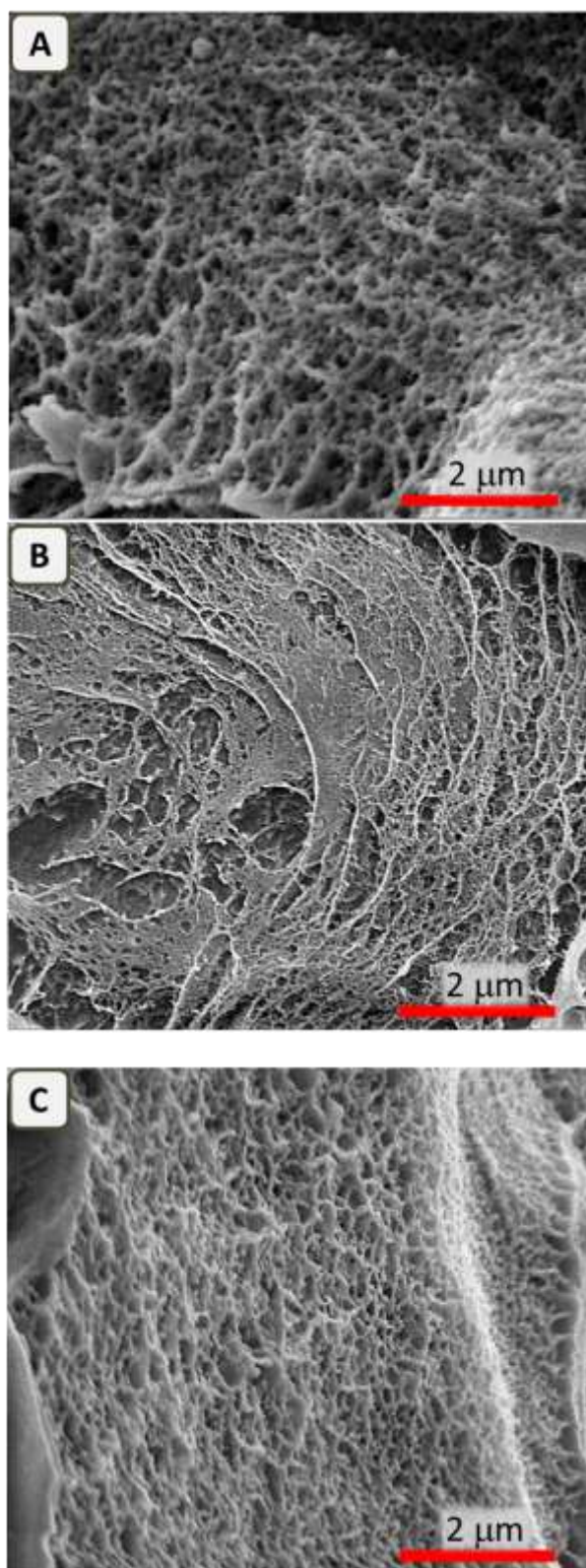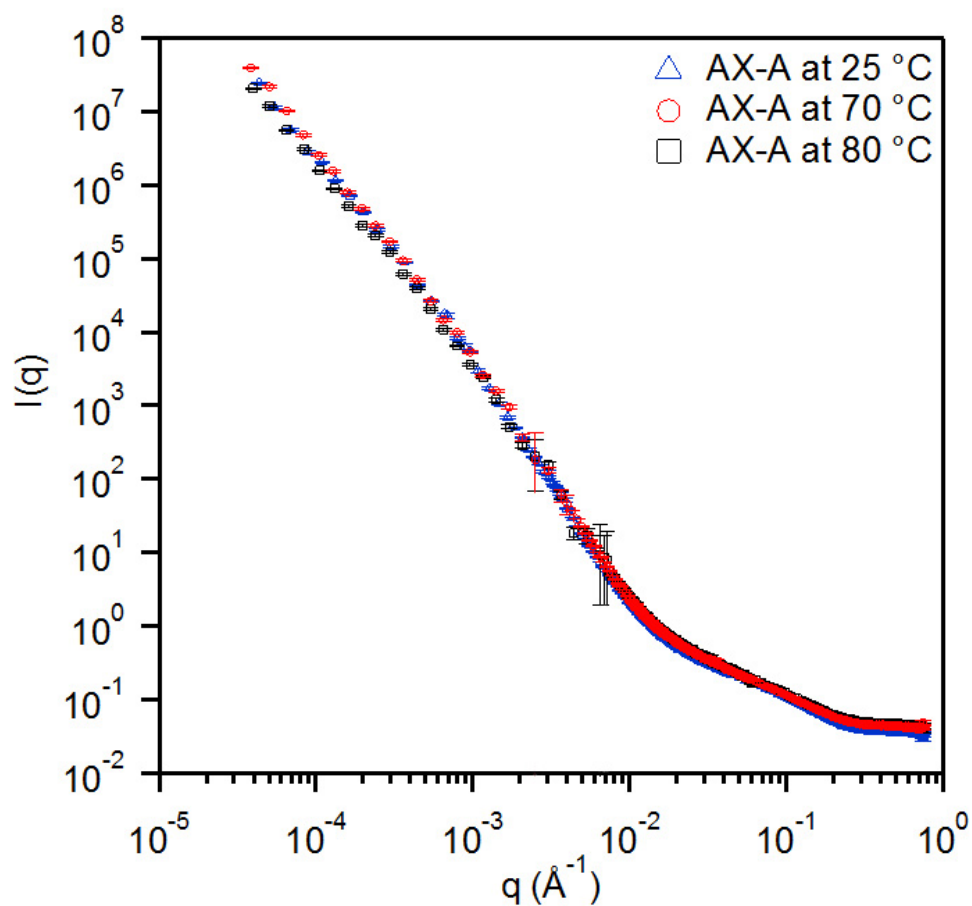
685

686

687

688

689

690

691

692

693

694

Supplementary Figure S2. SEM images of 5% AX-A ('A'), AX-W ('B') and AX-W-E (enzymatically treated AX-W fraction) ('C') in D_2O. In all images, the scale bar is 2 μm. The images show obvious signs of ice damage; however, they provide qualitative indication that the structure of *P.ovata* AX gels in D_2O and H_2O is similar.

Supplementary Figure S3. USAN/SANS data of AX-A from *P. ovata* seed mucilage in D$_2$O at 25 °C, 70 °C and 80 °C
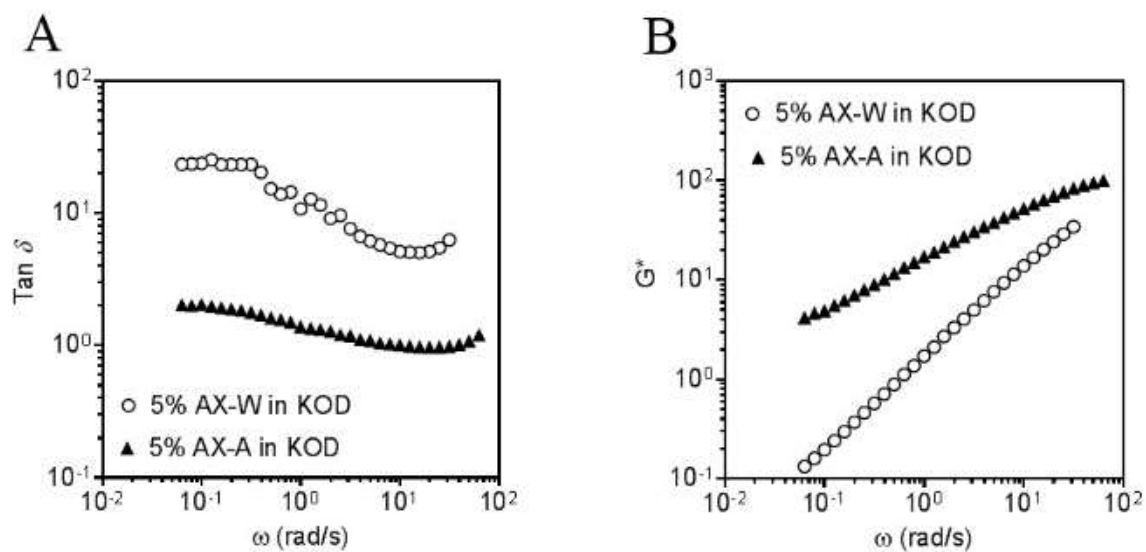
A

B

Supplementary Figure S4 The plot of tan δ against ω (A) and the plot of G* against ω (B).

708

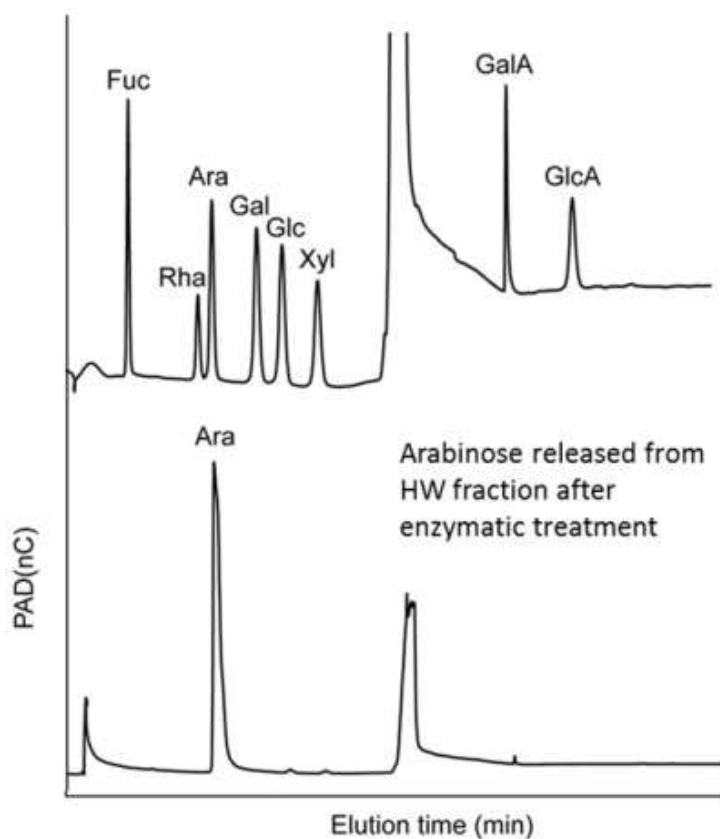709

710

711

712

713

714

715

716

717

718

719

720

721

722

Supplementary Figure S5. HPAEC-PAD chromatograph of standard monosaccharides, and monosaccharides released from AX-W fractions after α-L-arabinofuranosidase (*A. niger*) treatment. Adapted from Yu et al. (2017).

724

725

726

727

728

729

730

731

732